Revealing abnormal $\{11\bar{2}1\}$ twins in commercial purity Ti subjected to split Hopkinson pressure bar

Hailong Jia[a], Knut Marthinsen[a], Yanjun Li[a,*]

[a] Department of Materials Science and Engineering, Norwegian University of Science and Technology (NTNU), 7491 Trondheim, Norway

*Corresponding author: Yanjun Li, E-mail: <u>yanjun.li@ntnu.no</u>

Abstract

A commercial purity (CP) Ti alloy was subjected to high strain rate (~600 s^{-1}) compression deformation using a split Hopkinson pressure bar (SHPB) system. By multi-impacts, an accumulative deformation strain of ~0.15 was achieved. The microstructural evolution has been systematically analyzed by electron backscatter diffraction (EBSD). It is found that the CP-Ti alloy has been deformed predominantly by three different twinning modes, $\{10\bar{1}2\}$ (T1), $\{11\bar{2}1\}$ (T2) and $\{11\bar{2}2\}$ (C1). A large fraction of the $\{11\bar{2}1\}$ (T2) twin boundary (TB) segments are found to be in connection with deformation band (DB) boundary segments with misorientation angles much lower than the theoretical value of the $\{11\bar{2}1\}$ (T2) TB, ~35˚. Based on the analysis of the crystallographic nature of these abnormal $\{11\bar{2}1\}$ (T2) TBs and the calculation of Schmid factor, it is suggested that these abnormal $\{11\bar{2}1\}$ (T2) TBs are evolved from DB boundaries through the accumulative slip of single basal-⟨a⟩ dislocations, namely a kinking mechanism. This special twinning mode of the $\{11\bar{2}1\}$ (T2) twin has been attributed to the high strain rate deformation during SHPB compression.

Keywords: Deformation twins; Deformation bands; Basal slip; High strain rate; Titanium

1. Introduction

Deformation twinning has strong influences on the grain refinement [1], texture evolution [2-4] and mechanical behaviors [5-14] during plastic deformation of hexagonal close packed (HCP) alloys.

In the last decades, the occurrence of deformation twinning in HCP metallic materials under low speed deformation has been widely reported [15-18]. Different twinning modes can be activated, depending on the deformation temperature and the loading direction with respect to the c-axis of the unit cell. Four common deformation twinning systems have been reported in commercial purity (CP) Ti [15, 16, 19, 20], namely $\{10\bar{1}2\}$ $\langle\bar{1}011\rangle$ (T1), $\{11\bar{2}1\}$ $\langle\bar{1}\bar{1}26\rangle$ (T2), $\{11\bar{2}2\}$ $\langle11\bar{2}3\rangle$ (C1) and $\{10\bar{1}1\}$ $\langle10\bar{1}2\rangle$ (C2). Among these twins, $\{10\bar{1}2\}$ (T1) and $\{11\bar{2}1\}$ (T2) are tensile twins. This is because that generally these two twinning modes can be activated only in such grains with the c-axis strained in tension, resulting in extension of the crystal in the c-axis direction. Correspondingly, $\{11\bar{2}2\}$ (C1) and $\{10\bar{1}1\}$ (C2) are referred to as contraction twins. $\{10\bar{1}2\}$ (T1) and $\{11\bar{2}2\}$ (C1) are the most commonly observed twinning modes during deformation at room temperature (RT). Occasionally, $\{11\bar{2}1\}$ (T2) twins can also be observed in the cold-rolled CP-Ti [20, 21], while $\{10\bar{1}1\}$ (C2) twinning becomes the predominant twinning mode at elevated temperatures above 673 K [5, 22].

In addition to temperature [23, 24], it is well known that deformation mode of HCP metals and alloys can be significantly influenced by strain rate [24, 25]. However, studies on the deformation twinning behavior of Ti at high strain rates are less [26-31]. It has been found that the twining mode of Ti may be changed by the high strain rate deformation. For instance, during the dynamic plastic deformation (DPD) process (strain rate is ~4.5-5 × 10^2 s^{-1}), the $\{11\bar{2}4\}$ $\langle22\bar{4}\bar{3}\rangle$ (C3) twin could form in the high purity (99.99%) Ti, although its fraction is small (~5%) [32]. More $\{11\bar{2}4\}$ $\langle22\bar{4}\bar{3}\rangle$ (C3) twins was observed during ballistic impact deformation with a higher strain rate of ~10^3 s^{-1} [29]. However, the $\{11\bar{2}4\}$ $\langle22\bar{4}\bar{3}\rangle$ (C3) twins cannot be observed in samples deformed at quasi-static strain rates [32]. The deformation twins formed in CP-Ti subjected to split Hopkinson pressure bar (SHPB) under different strain rates of 10^3-10^4 s^{-1} have also been investigated [31]. It was demonstrated that the quantity of deformation twins at high strain rates was higher than that at low to medium strain rates.

In the classical theory of deformation twinning, the original (parent) lattice is re-orientated by atom displacements which are equivalent to a simple shear of the lattice points, or of some integral fraction of these points [24]. Interestingly, in a recent work on the CP-Ti subjected to DPD (drop hammer impact, strain rate $\sim 10^2$ s^{-1}) [30], some $\{11\bar{2}1\}$ (T2) twin boundaries (TBs) have been suggested to be formed by a special twinning mechanism, i.e., by a gradual evolution from deformation band (DB) boundaries through slip of single basal-$\langle a \rangle$ dislocations. In the present work, a CP-Ti alloy was subjected to compression deformation using SHPB. The evolution of microstructure, deformation twinning and texture has been studied. A special focus has been put on the analysis of the abnormal $\{11\bar{2}1\}$ (T2) TBs and their formation mechanism.

2. Experimental

A commercial purity Ti alloy (grade 1) with a chemical composition (wt.%) of 0.03 C, 0.0009 H, 0.008 N, 0.12 O, 0.06 Fe and Ti (in balance) was used in this study. The SHPB system has been shown in Fig. 1(a), which is a common technique for studying mechanical properties of materials subjected to high strain rate deformation by imparting a uniform and uniaxial load onto a sample. The diameter of the "input bar" and the "output bar" is 16 mm, both of which are made of steel. The steel bars have a density of 7850 kg/m^3 and the Young's modulus is $\sim$210 GPa. As shown in Fig. 1(b), cylindrical samples with a diameter of 10 mm and a height of 10 mm were designed to perform the SHPB tests. The high strain rate compression tests were carried out at RT. The deformation strain is defined as $\varepsilon = \ln(L_0/L_f)$, where L_0 and L_f are the initial and final height of the as-deformed sample, respectively. Multi-impacts were applied to samples to obtain different deformation strains. As indicated in Fig. 1(b), microstructures were investigated on the compression-radial (CD-RD) plane of as-deformed samples by electron backscatter diffraction (EBSD). The samples for EBSD were prepared by standard metallographic techniques followed by electro-polishing. EBSD was performed by using a Hitachi SU-6600 field emission gun SEM equipped with a Nordif EBSD detector and the TSL OIM software. Vickers hardness measurements were conducted using a DKV-1S Vickers

hardness testing machine under a load of 1 kg with a loading time of 15 s. The hardness values were averaged from six separate measurements.
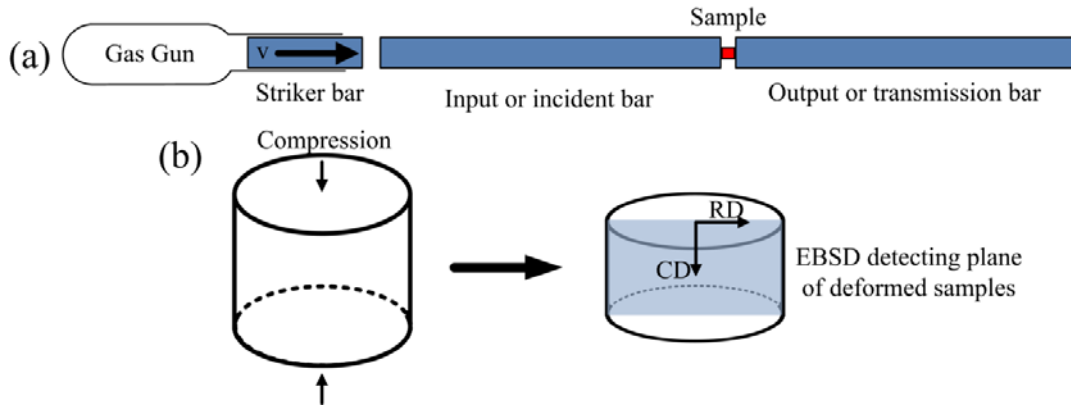

Fig. 1. (a) Schematic of the split Hopkinson pressure bar (SHPB) apparatus, and (b) illustration of the observation plane for EBSD. CD and RD are abbreviations for the compression and radial direction, respectively.

3. Results

3.1. The initial microstructure

The initial microstructure (before the compression deformation), as well as the $\{0001\}$ and $\{10\bar{1}0\}$ pole figures are shown in Fig. 2. As shown in Fig. 2(a), prior to deformation, the initial material comprises the single phase of α-Ti, with an equiaxed grain structure. The average grain size was measured to be ~20 μm. Furthermore, the material is twin-free, which can also be confirmed by the misorientation angle distribution chart (Fig. 2(b)), i.e., no preferred misorientation angles. As can be seen from the <0001> pole figure (Fig. 2(c)), the peak intensities (~4 times random) indicate that the c-axes of a large fraction of grains lie in the range of 60˚-90˚ to the CD. From the <10$\bar{1}$0> pole figure, it can be seen that there is no obvious preferential alignment of the <10$\bar{1}$0> directions with respect to the CD.
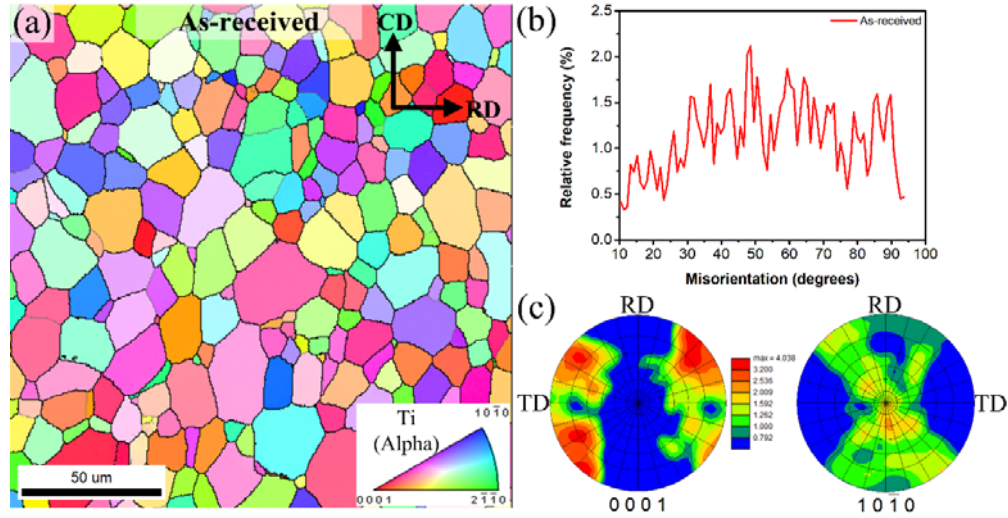
4

Fig. 2. (a) Initial microstructure of CP-Ti, (b) distribution of boundary misorientation angles of the as-received sample, and (c) {0001} and {10$\bar{1}$0} pole figures.

3.2. Hardness and strain rate

The evolution of the height of the sample and hardness as a function of the impact number has been plotted in Fig. 3(a). It can be seen that with increasing impact numbers, the height reduction rate decreases. It means that during deformation, grain refinement and work hardening make it more difficult to be deformed with further increased strains, which is consistent with the hardness evolution. When the strain is larger than ~0.07, the increase rate of hardness becomes much lower, which implies that the grain refinement rate, as well as the accumulation rate of dislocations is lower than that at low strains.

Fig. 3(b) shows the evolution of strain rate, engineering stress and engineering strain curves as a function of time for the ε = 0.073 sample. It can be seen that the initial strain rate is very high, with a maximum value of ~6 × 10^2 s^{-1}. As can be observed from Fig. 3(c), the maximum true stress of the ε = 0.073 sample is ~770 MPa. This result is similar to that of a CP-Ti alloy with a grain size of 35 μm (~750 MPa at ε ≈ 0.07), which was deformed at a strain rate of 4.5 × 10^3 s^{-1} using SHPB [33]. However, it is much lower in comparison to that of the ultrafine grained CP-Ti (~1150 MPa) with a grain size of ~260 nm deformed at a strain rate of ~4.3 × 10^3 s^{-1} using SHPB [33].
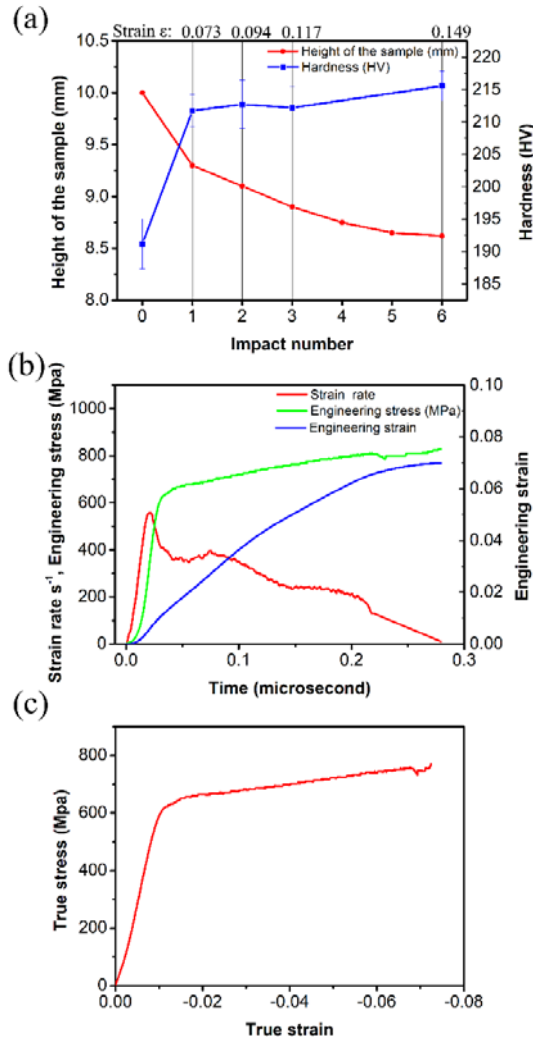
5

Fig. 3. (a) The height of the sample and hardness as a function of the impact number, (b) the evolution of strain rate, engineering stress and engineering strain as a function of time for the ε = 0.073 sample, and (c) the corresponding true stress-strain curve of the ε = 0.073 sample.

3.3. Deformation microstructure

3.3.1. Twins formed in samples deformed by SHPB

The rotation axes and misorientation angles of the four common deformation twin systems, including T1, T2, C1 and C2, have been summarized in Table 1 [29]. EBSD results of the as-deformed samples are shown in Fig. 4, where different kinds of TBs are indicated by different colors. In the OIM software, the maximum permitted deviation of the TB misorientation angles is set to be 1°. As can be seen, some grains are deformed by twinning intensively and others are much less. Within

6

grains, low angle boundaries are few, which means that deformation twinning is the dominant deformation mechanism. The formation of deformation twins and their intersections divide the grains into several smaller grains, resulting in significant grain refinement. In turn, this leads to a gradual decrease in the twinning ability. Thus, dislocation slip becomes dominate at high strain levels [19, 34]. Overall, similar to the results in Ref. [35], double twinning can rarely be seen. Only three twin types can be observed, i.e., $\{10\bar{1}2\}$ (T1), $\{11\bar{2}1\}$ (T2) and $\{11\bar{2}2\}$ (C1) twins. However, no $\{11\bar{2}4\}$ (C3) twins can be observed in the present CP-Ti alloy, which is different from the results in Refs. [29, 32]. The twining modes shown in the present sample are similar to that in room temperature rolled CP-Ti [4].

Table 1. Four common twin systems in Ti [29].

Type	Twin system	Misorientation axis/angle (for c/a = 1.588)	Shear magnitude
Tension twin (T1)	$\{10\bar{1}2\}\,\langle\bar{1}011\rangle$	$\langle11\bar{2}0\rangle$ 85.0°	0.174
Tension twin (T2)	$\{11\bar{2}1\}\,\langle\bar{1}\bar{1}26\rangle$	$\langle10\bar{1}0\rangle$ 35.0°	0.630
Contraction twin (C1)	$\{11\bar{2}2\}\,\langle11\bar{2}\bar{3}\rangle$	$\langle10\bar{1}0\rangle$ 64.4°	0.219
Contraction twin (C2)	$\{10\bar{1}1\}\,\langle10\bar{1}\bar{2}\rangle$	$\langle11\bar{2}0\rangle$ 57.2°	0.099

As shown in the boundary maps (Fig. 4), the fraction of $\{10\bar{1}2\}$ (T1) TBs (in red color) is much higher than $\{11\bar{2}2\}$ (C1) and $\{11\bar{2}1\}$ (T2) TBs. The formation of large amounts of $\{10\bar{1}2\}$ (T1) twins can be partly attributed to the crystallographic orientation of the parent grains (or initial texture), i.e., as shown in Fig. 2(c), c-axes of most grains lie in the range of 60˚-90˚ to the compression direction. Thus, during compression deformation, these grains are subjected mainly to extension along the c-axis, which promotes the formation of tensile twins: $\{10\bar{1}2\}$ (T1) and $\{11\bar{2}1\}$ (T2). Furthermore, as shown in Table 1, the shear magnitude of the $\{10\bar{1}2\}$ (T1) twin is relatively lower in comparison to the other twining modes (T2 and C1) [29]. Thus, for a given imposed strain along the planes with the maximum shear stress, a relatively large fraction of $\{10\bar{1}2\}$ (T1) twins have to be created to accommodate the imposed strain.
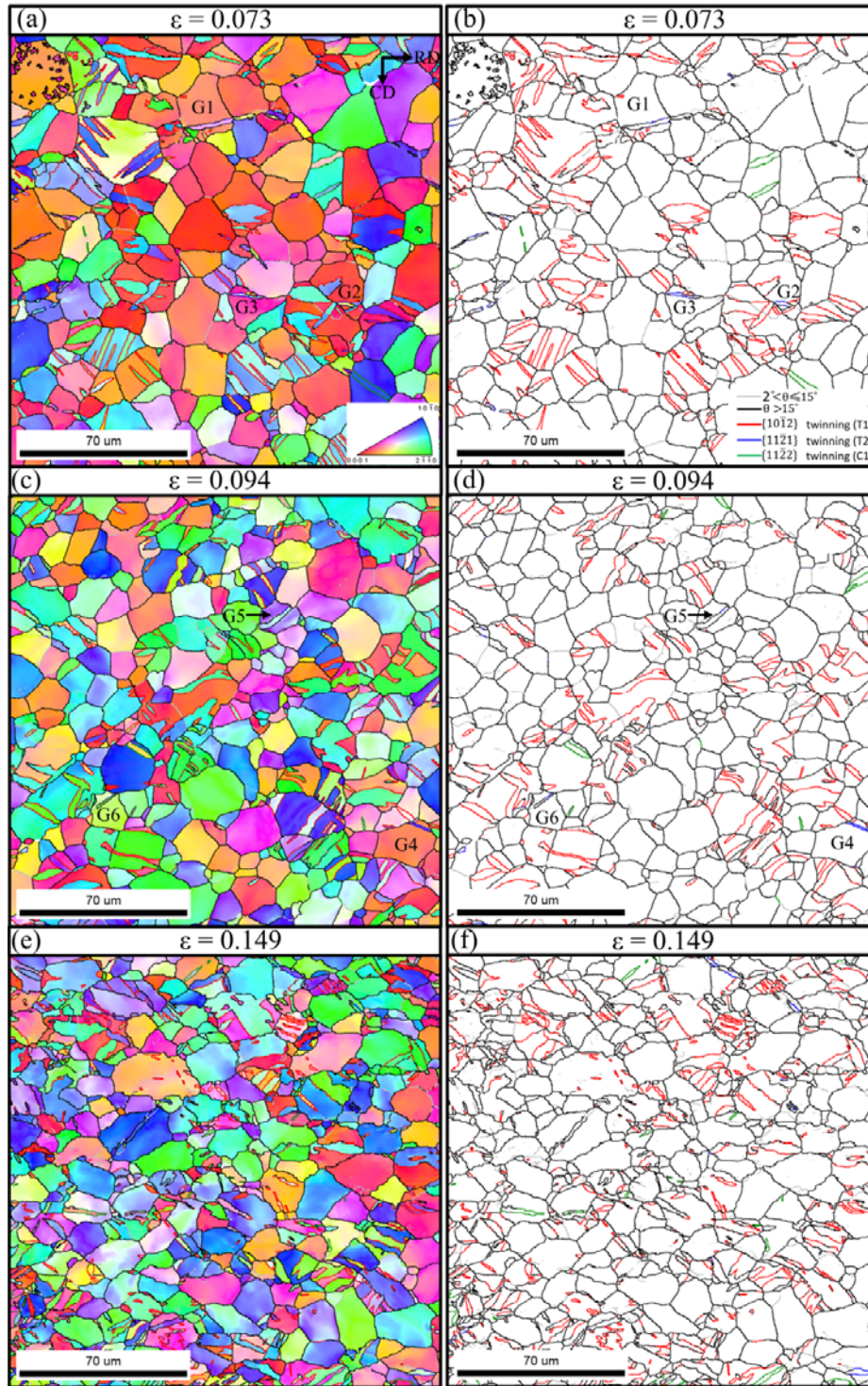
Fig. 4. EBSD orientation maps and grain boundary maps of as-deformed Ti samples. (a) and (b) $\varepsilon = 0.073$; (c) and (d) $\varepsilon = 0.094$; (e) and (f) $\varepsilon = 0.149$.

It can be seen that most of the $\{10\bar{1}2\}$ (T1) and $\{11\bar{2}2\}$ (C1) twin crystals show an elongated lenticular morphology, which can be attributed to faceted step-terrace structure of TBs [17]. In some grains, due to the formation of different variants of $\{10\bar{1}2\}$ (T1) twins, the $\{10\bar{1}2\}$ (T1) twin crystals show different aligning directions. It is interesting to see that in some grains, both the $\{10\bar{1}2\}$ (T1) and $\{11\bar{2}1\}$ (T2) twins can be observed, implying that the grains are with orientations favorable for the formation of both of the tension twins. For example, grains G1-G3 in Fig. 4(b).

A careful examination of the $\{11\bar{2}1\}$ (T2) twins shows that two different types of $\{11\bar{2}1\}$ (T2) TBs exist: (i) typical continuous TBs surrounding the lenticular $\{11\bar{2}1\}$ (T2) twins, like G4 in Fig. 4(d), and (ii) discontinuous $\{11\bar{2}1\}$ (T2) TB segments connected with deformation band (DB) boundaries with misorientation angles far away from that of the $\{11\bar{2}1\}$ (T2) TB, such as G5 and G6 in Fig. 4(d). To show these two types of $\{11\bar{2}1\}$ (T2) TB structures more clearly, G4-G6 have been enlarged and shown in Fig. 5. Fig. 5(a) shows the typical continuous and symmetrical $\{11\bar{2}1\}$ (T2) TB. G5 and G6 in Fig. 5(b) and (c) show the second type of $\{11\bar{2}1\}$ (T2) TB. It can be seen that misorientation angles of these non-T2 DB boundaries are much less than the theoretical misorientation angle value (~35°) of the $\{11\bar{2}1\}$ (T2) twin.
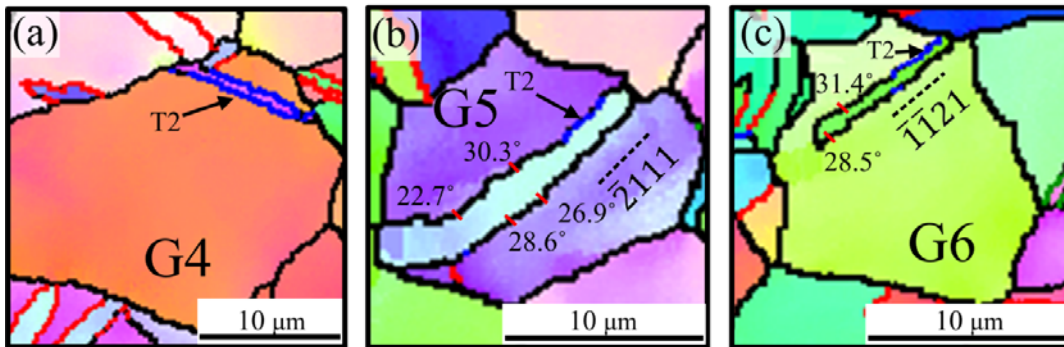

Fig. 5. Enlarged orientation maps of grains G4-G6 in Fig. 4(d), containing $\{11\bar{2}1\}$ (T2) TBs. (a) G4, (b) G5, and (c) G6.

Misorientation angle distribution of grain boundaries and TB fraction of different twins have been calculated from the EBSD data and shown in Fig. 6(a) and (b), respectively. As can be seen from Fig. 6(a), in the $\varepsilon = 0.073$ sample, four significant misorientation angle peaks can be seen at around 30˚, 34˚, 65˚ and 86˚, respectively. With increasing strains, only three peaks can be observed at around 34˚-35˚, 65˚ and 86˚, which are supposed to correspond to the 35.0˚ $\langle10\bar{1}0\rangle$ (T2), 64.4˚ $\langle10\bar{1}0\rangle$ (C1) and 85.0˚ $\langle2\bar{1}\bar{1}0\rangle$ (T1) TBs, respectively. As revealed by the spread/broadening of the peak at the right side of 85˚, the misorientation angles of $\{10\bar{1}2\}$ (T1) TBs become larger at large strains. It is interesting to see that at small strains, the misorientation angle peak corresponding to $\{11\bar{2}1\}$ (T2) TBs is smaller than the theoretical value (35.0˚). As the strain increases, the peak around 30˚ moves towards 35˚. This is in contrast to the misorientation peaks corresponding to the $\{10\bar{1}2\}$ (T1) and $\{11\bar{2}2\}$ (C1) TBs, which are always close to the theoretical values. In the previous work by Bozzolo et al. [20], a misorientation peak at 41˚ $\langle5\bar{1}\bar{4}3\rangle$ was observed in a cold-rolled CP-Ti. It was supposed that this misorientation peak belongs to the boundaries between one of the $\{11\bar{2}2\}$ (C1) variants and one of the $\{10\bar{1}2\}$ (T1) variants occurring in the same grains, or the boundaries between the primary and secondary twins (C1 inside the T1 primary twin or T1 inside the C1 primary twin). Here, no peak around 41˚ was found in this work, which can be related to the small amount of $\{11\bar{2}2\}$ (C1) TBs and rare double twinning.

The TB fraction of different twins has been calculated as the ratio between the length of each TB to the total length of all types of grain boundaries with misorientations > 5˚. As shown in Fig. 6(b), the fraction of $\{10\bar{1}2\}$ (T1) twins are much higher than others, confirming that the $\{10\bar{1}2\}$ (T1) twins are much easier to form than other types of twins at small strains. The fraction of $\{10\bar{1}2\}$ (T1) and $\{11\bar{2}2\}$ (C1) TBs shows a maximum at $\varepsilon = 0.073$ (one impact deformation), and then decreases with

increasing deformation strains. A maximum fraction (~2.2%) of the $\{11\bar{2}1\}$ (T2) TBs was obtained

after deformation of 2 impacts, $\varepsilon = 0.094$. By comparing to the maximum fraction (~0.8% at the strain

level, $\varepsilon = 0.29$) of the $\{11\bar{2}1\}$ (T2) TBs forming in a CP-Ti subjected to the DPD process (strain rate $<$

10^2 s^{-1}) [30], it can be concluded that the higher strain rate SHPB deformation favors the formation of
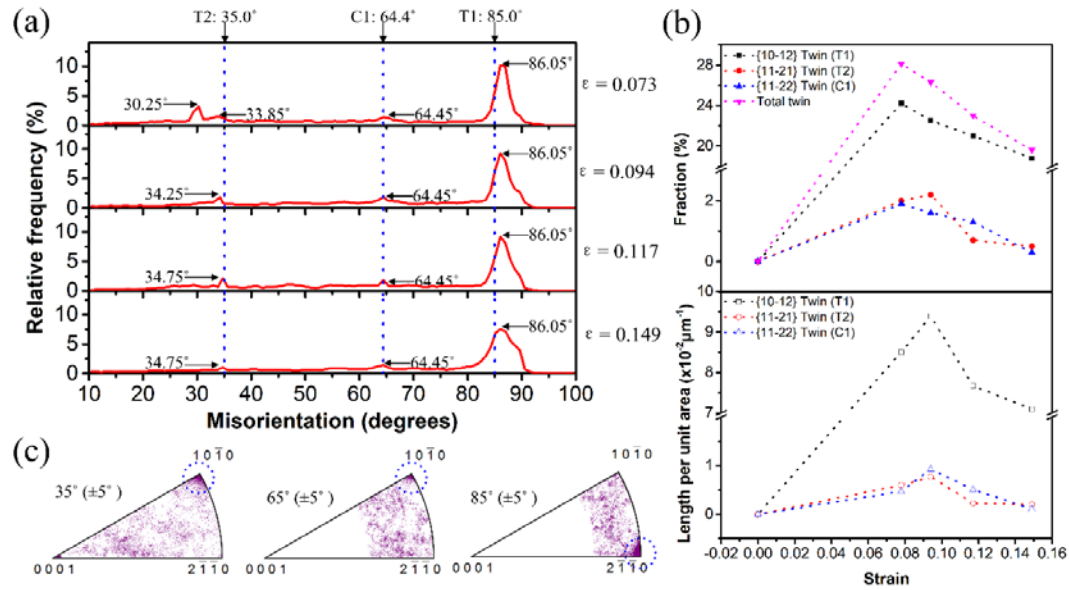
$\{11\bar{2}1\}$ (T2) TBs.

Fig. 6. (a) Misorientation angle distribution of grain boundaries in the as-deformed samples, (b) TB fraction among all grain boundaries (with misorientation angles $> 5°$) and length of TB per unit area as a function of strain, and (c) inverse pole figures showing the misorientation axis of boundaries with selected misorientation angles in the $\varepsilon = 0.149$ sample.

The reduction of TB fractions of all the three twin types with further increasing deformation strains can be attributed to the following factors. Firstly, with grain refinement during deformation, twinning becomes more difficult due to the increased critical shear stress for the twining activation [24, 36]. Secondly, twins can grow and sweep through the entire area of parent grains [37, 38], reducing the length of TBs. Lastly, the loss of twin orientation relationship of twins due to dislocation slip during further straining [39] can also result in the drop of TB length per unit area (Fig. 6(b)). As shown in Fig. 6(c), the loss of twin orientation relationship can be revealed by the misorientation axis

distribution of boundaries with misorientations around the three peaks in the $\varepsilon = 0.149$ sample. As indicated by the blue dotted circles, only part of the boundaries are with misorientation axes of $\langle 10\bar{1}0 \rangle$ (T2), $\langle 10\bar{1}0 \rangle$ (C1) and $\langle 2\bar{1}\bar{1}0 \rangle$ (T1), respectively.

3.3.2. Characteristic and formation of T2 twin boundaries

The evolution of both the misorientation angle and TB fraction indicates that the formation of the $\{11\bar{2}1\}$ (T2) TBs is different from the $\{10\bar{1}2\}$ (T1) and $\{11\bar{2}2\}$ (C1) TBs. As mentioned above, a peculiar characteristic of the $\{11\bar{2}1\}$ (T2) TBs is that a large fraction of them are connected to non-T2 DB boundaries. Fig. 7(a) and (b) show two examples of such $\{11\bar{2}1\}$ (T2) twins in G6 and G7, where only some boundary segments surrounding the twin-like DBs were automatically indexed as $\{11\bar{2}1\}$ (T2) TBs by the OIM software. The orientation relationship between the DB and the surrounding matrix can be determined by the pole figures shown in Fig. 7(c) and (d). It can be seen that the DB shares a common rotation axis of $\langle 10\bar{1}0 \rangle$ with the surrounding grain matrix, as marked by the blue dashed circle in the $\{10\bar{1}0\}$ pole figures. Furthermore, as indicated in the $\{11\bar{2}1\}$ pole figures, the DB and the surrounding grain matrix have a pair of coincident $\{11\bar{2}1\}$ planes.

As shown in Fig. 7(a) and (b), the $\{11\bar{2}1\}$ plane traces at the sample surface are indicated by the black dotted lines. The trace of the boundaries between the DB and matrix are parallel to the $\{11\bar{2}1\}$ plane traces, further confirming that the blue boundary segments are the $\{11\bar{2}1\}$ (T2) TBs. The measured local misorientation angles of the DB boundaries are shown in Fig. 7(e) and (f). It can be seen that the misorientation angles vary in the range of 27.3˚~35.9˚ and 28.5˚~35.0˚ for the left and right boundary of the DB6, respectively. For DB7, the misorientation angles of the right and left boundary of the DB are in the range of 22.1˚~30.4˚ and 18.3˚~36˚, respectively. It indicates that a large fraction of the DB boundary segments are not the $\{11\bar{2}1\}$ (T2) TBs. These features are significantly different from conventional deformation twins, of which the crystal rotation axis and

rotation angle are considered to be constant, because the shear plane and amount of shear are definitely defined by the geometrical relationships with respect to the grain matrix.
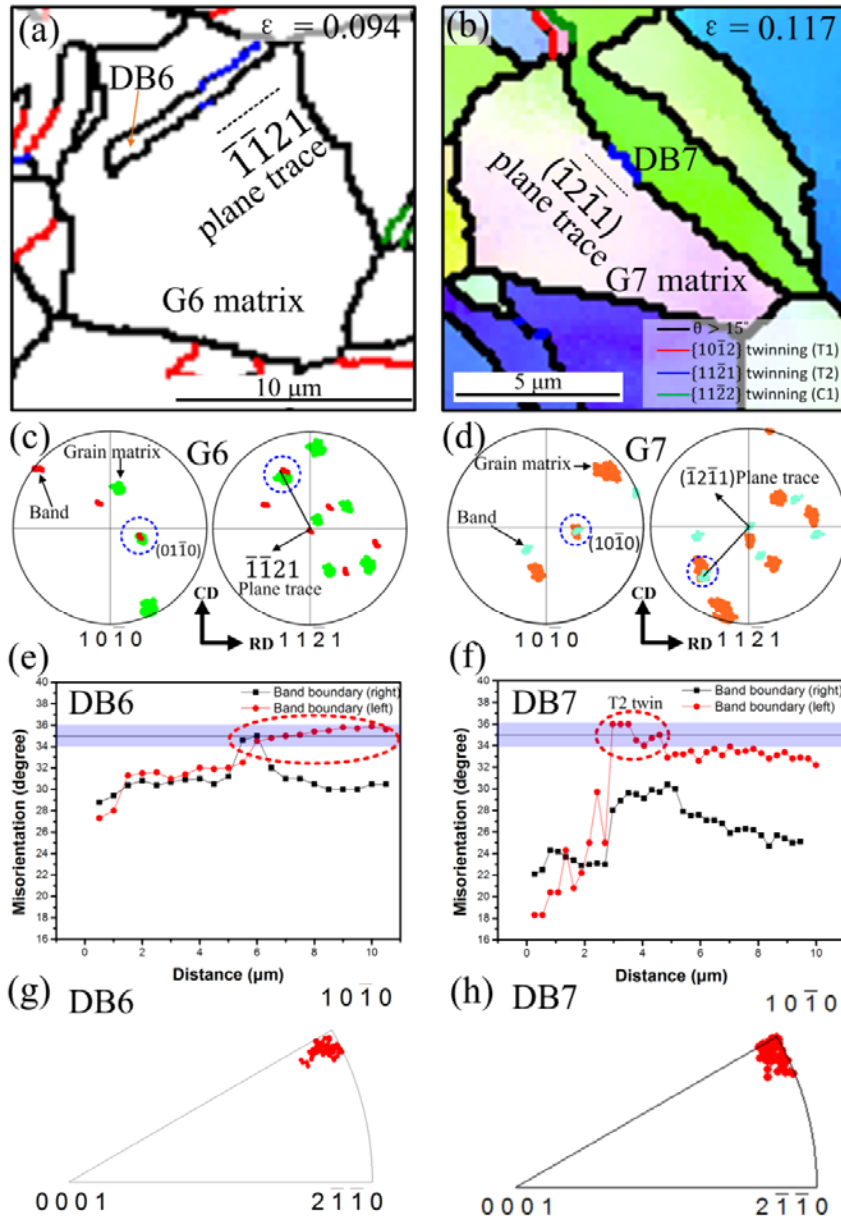

Fig. 7. (a) and (b) $\{11\bar{2}1\}$ (T2) twin boundaries within grains G6 and G7; (c) and (d) $\{10\bar{1}0\}$ and $\{11\bar{2}1\}$ pole figures for the DB and surrounding grain matrix; (e) and (f) misorientation distribution along the DB boundaries; (g) and (h) inverse pole figure showing the misorientation axes of DB boundaries.

Since the samples were subjected to mono-directional impact loading during SHPB, it is impossible to destroy the twin orientation relationship of the $\{11\bar{2}1\}$ (T2) TB by reducing the misorientation angle (such as from 35° to 27° and from 35° to 22° in Fig. 7(e) and (f), respectively) while keeping the same rotation axis as well as keeping the same $\{11\bar{2}1\}$ boundary planes unchanged. It is well known that the deformation TB can lose their perfect twin misorientation due to the different lattice rotation behaviors of the twin crystal and the matrix crystal caused by dislocation slip during further deformation after the twin formation. However, such a degradation of TBs usually causes the misorientation angles to increase instead of reduction [40]. This implies that DB boundaries with misorientation angles lower than 35° connected to $\{11\bar{2}1\}$ (T2) TBs are not the degradation result of the $\{11\bar{2}1\}$ (T2) TBs. Therefore, the $\{11\bar{2}1\}$ (T2) TB segments should have evolved gradually from the DB boundaries with lower misorientation angles based on a new TB formation mechanism.

A careful examination shows that a large number of twin-shaped DBs enclosed by boundaries of relatively low misorientation angles have already formed at a deformation strain as low as 0.073. Fig. 8(a) shows an example of such DBs inside the grain G8. As highlighted by the two pink circles, part of the DBs are with very low misorientation angles relative to the surrounding grain matrix, in the range of 4°-13°. Misorientation angles (> 15°) along boundaries of Band 1 and Band 2 were measured and plotted in Fig. 8(b). It shows that among the DB boundaries of Band 1 and Band 2, some segments are with misorientation angles in the range of 34°-36° and are automatically indexed as $\{11\bar{2}1\}$ (T2) TBs. As can be seen from the poles encircled by the blue dotted circles in the $\{10\bar{1}0\}$ pole figure in Fig. 8(c) and (d), both of the Band 1 and Band 2 have a common $\langle 10\bar{1}0 \rangle$ rotation axis as the surrounding matrix. As indicated by the blue dashed circles in the $\{11\bar{2}1\}$ pole figures, the DB and the grain matrix have one set of common $\{11\bar{2}1\}$ planes, the trace of which is close to that of DB boundaries (Fig. 8(a)). The crystallographic characteristic of these DBs are the same as the deformation kink bands frequently observed in HCP metals, like Zn, Ti and Mg, subjected to

compression deformation [41-44], caused by single basal-⟨a⟩ dislocation slip and having rotation axes of ⟨10$\bar{1}$0⟩. Therefore, these DBs should have formed by the kinking mechanism, which can be specifically termed as deformation kink band. The existence of the {11$\bar{2}$1} (T2) TB segments in the DB boundaries indicates that DB boundaries can transform into {11$\bar{2}$1} (T2) TBs by the kinking mechanism.
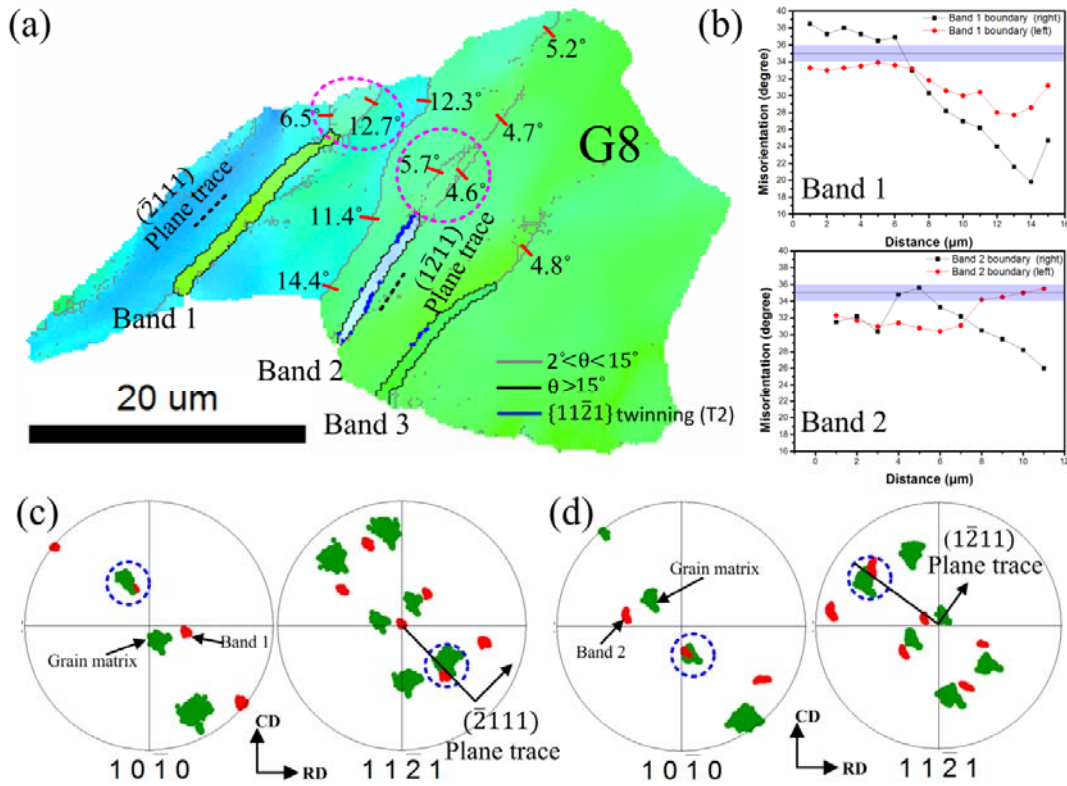

Fig. 8. (a) EBSD map of the grain G8 containing deformation bands in the ε = 0.073sample, (b) misorientation distribution along the DB boundaries (misorientations were measured from down to up), and (c) and (d) {10$\bar{1}$0} and {11$\bar{2}$1} pole figures for Band 1 and Band 2, respectively. The dash lines in (c) and (d) indicate the traces of {11$\bar{2}$1} planes of grain matrix crystals surrounding deformation bands.

3.4. Texture evolution

Fig. 9(a)-(e) display the evolution of inverse pole figures with respect to the compression direction as a function of deformation strains, by which the texture evolution of the material can be

15

evaluated. As can be seen from the inverse pole figure of the original microstructure (Fig. 9(a)), the texture component distributes mainly around the corner region between $[10\bar{1}0]\|CD$ and $[2\bar{1}\bar{1}0]\|CD$, while few grains have the [0001] direction parallel with the CD.
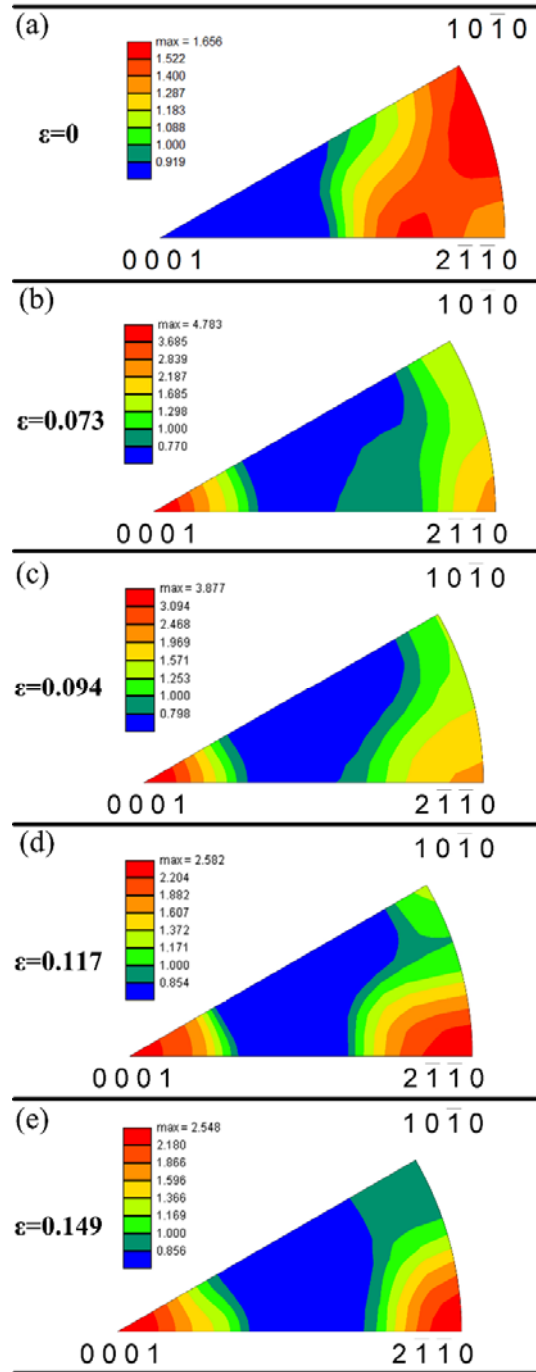

Fig. 9. Inverse pole figures with respect to the CD. (a) ε = 0, (b) ε = 0.073, (c) ε = 0.094, (d) ε = 0.117 and (e) ε = 0.149.

At ε = 0.073, as shown in Fig. 9(c), two clear texture components [0001]∥CD and [2$\bar{1}$$\bar{1}$0]∥CD have formed, each of which corresponds to a specific orientation within the as-deformed microstructure. The texture components [0001]∥CD should be attributed to the activation of {10$\bar{1}$2} (T1) twinning [3, 23] in those grains with c-axes having a large angle to the CD. Due to this tensile twinning mode, the grains are rotated by 85° around the ⟨11$\bar{2}$0⟩ axes, so that the [0001] directions of the newly formed twin crystals are close to the CD. With increasing the strain (Fig. 9(d)-(e)), the intensity of the texture component [2$\bar{1}$$\bar{1}$0]∥CD becomes strengthened at the expense of the texture component [0001]∥CD , which could be due to dislocation slip. It implies that the deformation of CP-Ti has been mainly through ⟨a⟩ dislocation slip at higher deformation strains. As a result, some of the grains will gradually rotate to a stable orientation, namely with one of the ⟨2$\bar{1}$$\bar{1}$0⟩ directions parallel with the CD.

4. Discussion

The {11$\bar{2}$1} (T2) TBs shown in Fig. 7 are similar to those reported in Ref. [30], in which the CP-Ti was subjected to the drop hammer deformation with a strain rate < 10^2 s^{-1}. The {11$\bar{2}$1} (T2) TB formation mechanism was suggested as a gradual evolution from DB boundaries through slip of single basal-⟨a⟩ dislocations [30], which is different from conventional twinning mechanisms.

In order to check that the abnormal {11$\bar{2}$1} (T2) twins and DBs have formed through the same kinking mechanism, the possible active dislocation slip systems have been evaluated by calculating the Schmid factor (SF) of the DB and the surrounding grain matrix crystals. In Ti, since the critical resolved shear stress (CRSS) for the basal-⟨a⟩ slip and prismatic-⟨a⟩ slip is much lower than the pyramidal-⟨a+c⟩ slip, they are much easier to be activated during room temperature deformation [18, 45, 46]. Therefore, in the present study, only SF values of basal-⟨a⟩ and prismatic-⟨a⟩ dislocation slip systems are calculated and the slip systems with SF > 0.3 are arbitrarily considered to possess a high

possibility to be activated during deformation. Table 2 shows the calculated SF values of grains G6 and G7 in Fig. 7.

Table 2. Schmid factors (SFs) for basal-⟨a⟩ and prismatic-⟨a⟩ slip systems of grains G6 and G7 in Fig. 7.

		G6 matrix	DB6	G7 matrix	DB7
	$(0001)[\bar{1}\,\bar{1}\,20]$	0.26	0.26	0.28	0.13
Basal-⟨a⟩ slip systems	$(0001)[\bar{1}\,2\,\bar{1}\,0]$	0.22	0.20	**0.50**	**0.41**
	$(0001)[2\bar{1}\,\bar{1}\,0]$	**0.48**	**0.46**	0.22	0.28
	$(1\bar{1}00)[11\bar{2}0]$	0.03	0.14	0.22	0.07
Prismatic-⟨a⟩ slip systems	$(10\bar{1}0)[1\bar{2}10]$	0.26	0.12	0.03	0.05
	$(0\bar{1}10)[\bar{2}110]$	0.29	0.02	0.19	0.11

As indicated, for G6 and G7, the SFs of all the prismatic slip systems both in the grain matrix and DBs are less than 0.3. On the other hand, both the grain matrix and the DB in the two grains have a basal-⟨a⟩ slip variant with SF value larger than 0.4. It suggests that prismatic-⟨a⟩ slip is suppressed in both G6 and G7 while the deformation is carried by the single basal-⟨a⟩ slip. It is known that during kinking, the rotation axis of the crystal within the DB will be perpendicular to both the slip plane normal and the Burger's vector of the basal-⟨a⟩ dislocation. Thus, the rotation axis of DB6 and DB7 will be $[01\bar{1}0]$ and $[10\bar{1}0]$, respectively. This is consistent with the crystal rotation axes measured directly from EBSD maps (Fig. 7(c) and (d)). Accordingly, the DB6 and DB7 have formed by kinking due to the single basal-⟨a⟩ dislocation slip, which has the maximum SF value. This is consistent with the first principles calculation results by Lane et al. [41], where the $\{11\bar{2}1\}$ (T2) twin can form by the glide of basal-⟨a⟩ dislocations.

Fig. 10 shows a schematic drawing for the formation of the $\{11\bar{2}1\}$ (T2) TBs, where only one basal-⟨a⟩ slip system $(0001)[\bar{1}2\bar{1}0]$ is supposed to be activated. The lack of other active slip systems in this grain facilitates the formation of a DB by kinking during high strain rate deformation. As shown in Fig. 10(b), the boundary walls between the DB and grain matrix are constituted of numerous basal-

⟨a⟩ dislocations [41, 42]. On the other hand, the operation of the single (0001) [$\bar{1}2\bar{1}0$] slip in the DB and grain matrix induces the lattice rotation around the same axis of [$10\bar{1}0$], but in opposite directions.
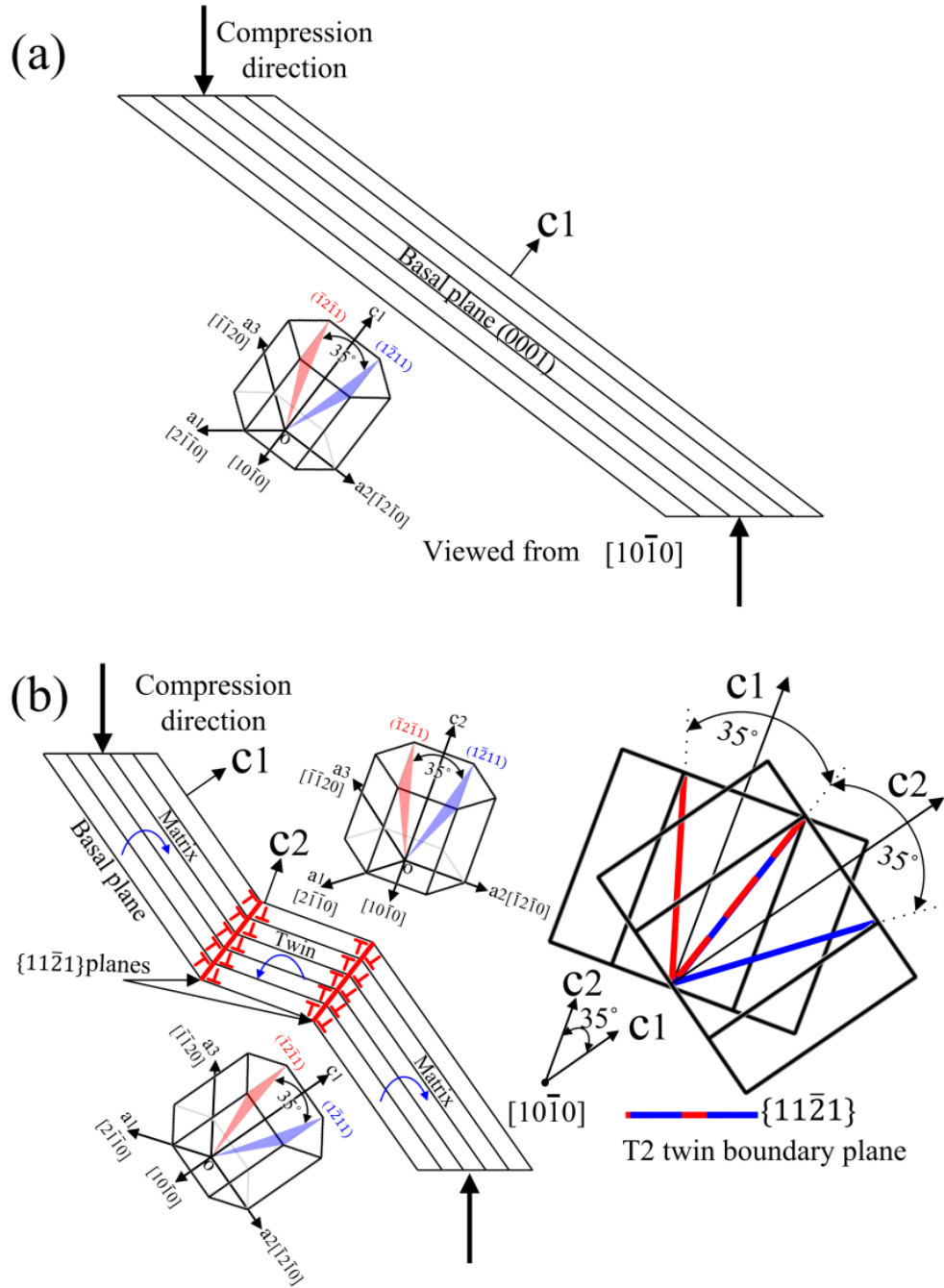

Fig. 10. Illustration for the formation of a DB by kinking (the DB boundary becomes a {11$\bar{2}$1} (T2) TB when the misorientation angle is 35˚).

When the angle between the grain matrix and the deformation kink band equals to 35˚, one of the $\{11\bar{2}1\}$ plane in the grain matrix becomes coincident with one of the $\{11\bar{2}1\}$ plane in the deformation kink band, forming the $\{11\bar{2}1\}$ (T2) TB. Due to the high strain rate and the mono-directional loading nature of the SHPB process, once a single basal-⟨a⟩ dislocation slip is activated, it may continue until the impact loading is finished, which has been shown to be possible in Ref. [30]. This work confirms the formation of the $\{11\bar{2}1\}$ (T2) TB through the "twinning by kinking" mechanism. It seems that such a twinning mechanism is favorable during the high strain rate deformation.

5. Conclusions

The deformation twins formed in a CP-Ti subjected to SHPB have been carefully studied. After deformation, three types of deformation twins have formed, namely, $\{10\bar{1}2\}$ ⟨$\bar{1}011$⟩ (T1), $\{11\bar{2}1\}$ ⟨$\bar{1}\bar{1}$ 26⟩ (T2) and $\{11\bar{2}2\}$ ⟨$11\bar{2}\bar{3}$⟩ (C1). Specifically, an intriguing phenomenon that a large fraction of $\{11\bar{2}1\}$ (T2) TBs connected to non-T2 DB boundaries with low misorientation angles (< 35˚) were observed. The present work has confirmed that the $\{11\bar{2}1\}$ (T2) TBs can be evolved from DB boundaries through a gradual increase in misorientation angles. This is caused by the kinking mechanism, i.e., accumulative slip of single basal-⟨a⟩ dislocations, which has been verified by the Schmid factor calculation. It is supposed that the special deformation mode of SHPB in terms of high strain rate and mono-directional impact loading plays an important role in the formation of the abnormal $\{11\bar{2}1\}$ (T2) TBs. The high strain rate deformation favors the occurrence of abnormal $\{11\bar{2}1\}$ (T2) TBs.

Acknowledgements

References

[1] K. Lu, N. Hansen, Structural refinement and deformation mechanisms in nanostructured metals, Scripta Materialia 60(12) (2009) 1033-1038.

[2] M.J. Philippe, C. Esling, B. Hocheid, Role of Twinning in Texture Development and in Plastic Deformation of Hexagonal Materials, Textures and Microstructures 7(4) (1988) 265-301.

[3] E.A. Calnan, C.J.B. Clews, XCIII. The development of deformation textures in metals.—Part III. Hexagonal structures, The London, Edinburgh, and Dublin Philosophical Magazine and Journal of Science 42(331) (1951) 919-931.

[4] Y.B. Chun, S.H. Yu, S.L. Semiatin, S.K. Hwang, Effect of deformation twinning on microstructure and texture evolution during cold rolling of CP-titanium, Materials Science and Engineering: A 398(1) (2005) 209-219.

[5] M.H. Yoo, Slip, twinning, and fracture in hexagonal close-packed metals, Metallurgical Transactions A 12(3) (1981) 409-418.

[6] M.R. Barnett, Twinning and the ductility of magnesium alloys, Materials Science and Engineering: A 464(1) (2007) 1-7.

[7] A.M. Garde, E. Aigeltinger, R.E. Reed-Hill, Relationship between deformation twinning and the stress-strain behavior of polycrystalline titanium and zirconium at 77 K, Metallurgical Transactions 4(10) (1973) 2461-2468.

[8] L. Rémy, The interaction between slip and twinning systems and the influence of twinning on the mechanical behavior of fcc metals and alloys, Metallurgical Transactions A 12(3) (1981) 387-408.

[9] A.A. Salem, S.R. Kalidindi, R.D. Doherty, Strain hardening of titanium: role of deformation twinning, Acta Materialia 51(14) (2003) 4225-4237.

[10] G.C. Kaschner, C.N. Tomé, I.J. Beyerlein, S.C. Vogel, D.W. Brown, R.J. McCabe, Role of twinning in the hardening response of zirconium during temperature reloads, Acta Materialia 54(11) (2006) 2887-2896.

[11] A.M. Garde, R.E. Reed-Hill, The importance of mechanical twinning in the stress-strain behavior of swaged high purity fine-grained titanium below 424°K, Metallurgical Transactions 2(10) (1971) 2885-2888.

[12] L. Lu, M.L. Sui, K. Lu, Superplastic Extensibility of Nanocrystalline Copper at Room Temperature, Science 287(5457) (2000) 1463-1466.

[13] L. Lu, Y.F. Shen, X.H. Chen, L.H. Qian, K. Lu, Ultrahigh strength and high electrical conductivity in copper, Science 304(5669) (2004) 422-426.

[14] K. Lu, L. Lu, S. Suresh, Strengthening Materials by Engineering Coherent Internal Boundaries at the Nanoscale, Science 324 (2009) 349-352.

[15] Y.J. Chen, Y.J. Li, J.C. Walmsley, S. Dumoulin, S.S. Gireesh, S. Armada, P.C. Skaret, H.J. Roven, Quantitative analysis of grain refinement in titanium during equal channel angular pressing, Scripta Materialia 64(9) (2011) 904-907.

[16] Y.J. Chen, Y.J. Li, J.C. Walmsley, S. Dumoulin, P.C. Skaret, H.J. Roven, Microstructure evolution of commercial pure titanium during equal channel angular pressing, Materials Science and Engineering: A 527(3) (2010) 789-796.

[17] Y.J. Li, Y.J. Chen, J.C. Walmsley, R.H. Mathinsen, S. Dumoulin, H.J. Roven, Faceted interfacial structure of {10-11} twins in Ti formed during equal channel angular pressing, Scripta Materialia 62(7) (2010) 443-446.

[18] A.A. Salem, S.R. Kalidindi, S.L. Semiatin, Strain hardening due to deformation twinning in α-titanium: Constitutive relations and crystal-plasticity modeling, Acta Materialia 53(12) (2005) 3495-3502.

[19] N. Stanford, U. Carlson, M.R. Barnett, Deformation Twinning and the Hall–Petch Relation in Commercial Purity Ti, Metallurgical and Materials Transactions A 39(4) (2008) 934-944.

[20] N. Bozzolo, L. Chan, A.D. Rollett, Misorientations induced by deformation twinning in titanium, Journal of Applied Crystallography 43(3) (2010) 596-602.

[21] L. Wang, R. Barabash, T. Bieler, W. Liu, P. Eisenlohr, Study of {11-21} Twinning in α-Ti by EBSD and Laue Microdiffraction, Metallurgical and Materials Transactions A 44(8) (2013) 3664-3674.

[22] N.E. Paton, W.A. Backofen, Plastic deformation of titanium at elevated temperatures, Metallurgical Transactions 1(10) (1970) 2839-2847.

[23] Z. Zeng, S. Jonsson, H.J. Roven, The effects of deformation conditions on microstructure and texture of commercially pure Ti, Acta Materialia 57(19) (2009) 5822-5833.

[24] J.W. Christian, S. Mahajan, Deformation twinning, Progress in Materials Science 39(1–2) (1995) 1-157.

[25] H.L. Jia, S.B. Jin, Y.J. Li, Formation of Σ3{110} incoherent twin boundaries through geometrically necessary boundaries in an Al-8Zn alloy subjected to one pass of equal channel angular pressing, Journal of Alloys and Compounds 762 (2018) 190-195.

[26] D.R. Chichili, K.T. Ramesh, K.J. Hemker, The high-strain-rate response of alpha-titanium: experiments, deformation mechanisms and modeling, Acta Materialia 46(3) (1998) 1025-1043.

[27] J. Cheng, S. Nemat-Nasser, A model for experimentally-observed high-strain-rate dynamic strain aging in titanium, Acta Materialia 48(12) (2000) 3131-3144.

[28] W. Huang, X. Zan, X. Nie, M. Gong, Y. Wang, Y. Xia, Experimental study on the dynamic tensile behavior of a poly-crystal pure titanium at elevated temperatures, Materials Science and Engineering: A 443(1) (2007) 33-41.

[29] S.J. Lainé, K.M. Knowles, {11-24} deformation twinning in commercial purity titanium at room temperature, Philosophical Magazine 95(20) (2015) 2153-2166.

[30] S.B. Jin, K. Marthinsen, Y.J. Li, Formation of {11-21} twin boundaries in titanium by kinking mechanism through accumulative dislocation slip, Acta Materialia 120 (2016) 403-414.

[31] T. Wang, B. Li, M. Li, Y. Li, Z. Wang, Z. Nie, Effects of strain rates on deformation twinning behavior in α-titanium, Materials Characterization 106 (2015) 218-225.

[32] F. Xu, X. Zhang, H. Ni, Q. Liu, {11-24} deformation twinning in pure Ti during dynamic plastic deformation, Materials Science and Engineering: A 541 (2012) 190-195.

[33] D. Jia, Y.M. Wang, K.T. Ramesh, E. Ma, Y.T. Zhu, R.Z. Valiev, Deformation behavior and plastic instabilities of ultrafine-grained titanium, Applied Physics Letters 79(5) (2001) 611-613.

[34] F. Xu, X. Zhang, H. Ni, Y. Cheng, Y. Zhu, Q. Liu, Effect of twinning on microstructure and texture evolutions of pure Ti during dynamic plastic deformation, Materials Science and Engineering: A 564 (2013) 22-33.

[35] N.P. Gurao, R. Kapoor, S. Suwas, Deformation behaviour of commercially pure titanium at extreme strain rates, Acta Materialia 59(9) (2011) 3431-3446.

[36] M.A. Meyers, O. Vöhringer, V.A. Lubarda, The onset of twinning in metals: a constitutive description, Acta Materialia 49(19) (2001) 4025-4039.

[37] Q. Ma, H. El Kadiri, A.L. Oppedal, J.C. Baird, B. Li, M.F. Horstemeyer, S.C. Vogel, Twinning effects in a rod-textured AM30 Magnesium alloy, International Journal of Plasticity 29 (2012) 60-76.

[38] F. Mokdad, D.L. Chen, D.Y. Li, Single and double twin nucleation, growth, and interaction in an extruded magnesium alloy, Materials & Design 119 (2017) 376-396.

[39] L. Wang, R.I. Barabash, Y. Yang, T.R. Bieler, M.A. Crimp, P. Eisenlohr, W. Liu, G.E. Ice, Experimental Characterization and Crystal Plasticity Modeling of Heterogeneous Deformation in Polycrystalline α-Ti, Metallurgical and Materials Transactions A 42(3) (2011) 626-635.

[40] Y.J. Chen, Y.J. Li, X.J. Xu, J. Hjelen, H.J. Roven, Novel deformation structures of pure titanium induced by room temperature equal channel angular pressing, Materials Letters 117 (2014) 195-198.

[41] N.J. Lane, S.I. Simak, A.S. Mikhaylushkin, I.A. Abrikosov, L. Hultman, M.W. Barsoum, First-principles study of dislocations in hcp metals through the investigation of the (11-21) twin boundary, Physical Review B 84(18) (2011) 184101.

[42] J. Hess, C. Barrett, Structure and nature of kink bands in zinc, Transactions of the American Institute of Mining and Metallurgical Engineers 185(9) (1949) 599-606.

[43] K. Hagihara, M. Yamasaki, M. Honnami, H. Izuno, M. Tane, T. Nakano, Y. Kawamura, Crystallographic nature of deformation bands shown in Zn and Mg-based long-period stacking ordered (LPSO) phase, Philosophical Magazine 95(2) (2015) 132-157.

[44] A.G. Crocker, J.S. Abell, The crystallography of deformation kinking, Philosophical Magazine 33(2) (1976) 305-310.

[45] J. Gong, A.J. Wilkinson, Anisotropy in the plastic flow properties of single-crystal α titanium determined from micro-cantilever beams, Acta Materialia 57(19) (2009) 5693-5705.

[46] A.T. Churchman, The Slip Modes of Titanium and the Effect of Purity on their Occurrence during Tensile Deformation of Single Crystals, Proceedings of the Royal Society of London. Series A, Mathematical and Physical Sciences 226(1165) (1954) 216-226.